PAPER

Liquid-phase deposition of ferroelectrically switchable nanoparticle-based BaTiO₃ films of macroscopically controlled thickness†

D. Erdem,[a] Y. Shi,[b] F. J. Heiligtag,[a] A. C. Kandemir,[c] E. Tervoort,[a] J. L. M. Rupp[b] and M. Niederberger*[a]

BaTiO₃ films are extensively used in many electrical devices, because they offer remarkable dielectric and ferroelectric properties. Here, we demonstrate a powerful, nanoparticle-based deposition route towards BaTiO₃ films with systematic thickness control over a wide range up to several microns. The unusual control over the film thickness with the maintenance of crack free nanostructures, phase and ferroelectric properties of the BaTiO₃ films allows us to fabricate various future devices of different thicknesses by a single deposition method. For this, films are deposited from stable dispersions of BaTiO₃ nanocrystals, synthesized *via* an efficient microwave-assisted non-aqueous sol–gel approach. Crack-free films of controlled thickness are obtained by a carefully elaborated, alternating process of spin-coating and intermediate drying. According to X-ray diffraction and confocal Raman microscopy, the final, sintered films consist of BaTiO₃ nanocrystals of about 20 nm in a hexagonal–tetragonal phase mixture. The nanoparticulate films display outstanding optical characteristics exceeding 90% transparency above 500 nm and a band gap of 3.5 eV. The latter, band gap, is larger than the classic bulk material's band gap of 3.2 eV, indicating a more electrically insulating nature of the films. Piezoresponse force microscopy gives evidence for potent ferroelectric switching. This newly accessible film processing route with wide film thickness tuning allows for desired ferroelectric response with the advantage of a wide film thickness to implicate building blocks for various applications *e.g.* ferroelectric random access memory devices, microelectromechanical system devices or Bragg reflectors.

Introduction

Driven by the rapid development of our digital information era and the demand for transfer and computation of data at low energy consumption, developing new functional thin film memory devices represents one of the major scientific challenges of our century. An important material in the pursuit of this quest is BaTiO₃, which has a variety of engineering applications such as high *k* dielectric in field effect transistors,[1,2] in ceramic capacitors,[3,4] ferroelectric based random access memory devices,[5] resistive random access memory devices,[6] microelectromechanical system (MEMS) devices, multiferroics[7–9] and planar Bragg reflector waveguides.[10,11] Among them, capacitor and memory based applications require thin films in sub-micron ranges due

to operation voltage[12] and information storage density concerns, whereas film devices of micrometer thicknesses are desired for MEMSs. In these applications the dielectric, ferroelectric and multiferroic responses exhibit pronounced size effects and it is important that the BaTiO₃ nanoparticles are larger than the ferroelectric limit.[13] Additionally, the composition should be phase pure to reach the targeted ferroelectric functionality.[14–16]

State-of-the-art BaTiO₃ deposition techniques succeed in producing nano-grained structures with large effective surface area to sample volume ratios. Yet, these methods are often restricted to the sub-micron film thickness ranges due to slow deposition rates and cost limitations.[17–19] In principle, wet chemistry-based approaches are superior to vacuum-based techniques in terms of costs.[20–23] However, traditional approaches such as the sol–gel technique or pyrolysis reveal severe limitations for films thicker than one micrometer due to solvent evaporation.[24] Additionally, they often show non-desired phases such as biphasic amorphous–crystalline structures[25] or difficulties in controlling the phase-stability.[26] The reason for all these problems in depositing a crack-free film is that pyrolysis, crystallization and grain growth

[a] *Multifunctional Materials, Department of Materials, ETH Zurich, 8093 Zurich, Switzerland. E-mail: markus.niederberger@mat.ethz.ch; Tel: +41 44 633 63 90*

[b] *Electrochemical Materials, Department of Materials, ETH Zurich, 8093 Zurich, Switzerland*

[c] *Nanometallurgy, Department of Materials, ETH Zurich, 8093 Switzerland*

† Electronic supplementary information (ESI) available. See DOI: 10.1039/c5tc02214b

This journal is © The Royal Society of Chemistry 2015

J. Mater. Chem. C, 2015, **3**, 9833–9841 | 9833

proceed in parallel, involving evaporation of solvents to drive the kinetics.[25] Cracking of the films due to internal crystallization processes and grain growth stresses are particularly pronounced above a critical film thickness, leading to failure in device processing. Therefore, the utilization of dispersions containing crystalline nanoparticles should represent a promising strategy to produce films with a greatly enlarged thickness range, because crystallization processes and the associated tensile stresses during sintering are avoided. In this aspect, doctor blading of nanocrystal slurries, assisted by plasticizers for green strength, performs well for micrometer thick films, but fails to produce films of nm thickness.[27] Other approaches to make nanocrystalline BaTiO$_3$ films with thicknesses from some tenths of nanometers to several microns include colloidal film deposition techniques such as spin and dip coating of nanocrystal dispersions. Typically, the dispersion media are organic due to their good substrate wetting properties and high volatility.[28] Although non-aqueous sol–gel methods often lead to well-dispersible nanoparticles and thus are widely employed,[29–32] additional surface functionalization with sterically stabilizing molecules to improve the stability of the dispersions might be required.[33]

However, this additional amount of organics introduces capillary stresses during its thermal removal, already resulting in premature cracking in films of just sub-micrometer thickness.[34,35]

While colloidal dispersion techniques have been applied to SiO$_2$,[36,37] TiO$_2$,[38,39] and SnO$_2$[40,41] based films with thicknesses in the sub-micron range, no deposition technique is available to produce one of the most relevant electroceramics, namely, BaTiO$_3$, with a broader range of film thicknesses. As a matter of fact, wet chemical deposition routes bridging the gap between the different methods and thus covering a broad range of thicknesses would be highly beneficial from a technical as well as from a scientific point of view (Fig. 1). Moreover, the integration of nanoparticle thin films into devices is often problematic and it is challenging to achieve the targeted functionality due to unwanted size effects and film quality issues related to impurities, surface roughness, porosity, cracks and other inhomogeneities.

In this paper, we describe a simple liquid phase deposition route towards BaTiO$_3$ films with controlled thicknesses up to the micron range using BaTiO$_3$ nanoparticle dispersions. Phase-pure BaTiO$_3$ nanoparticles with high crystallinity and larger than the ferroelectric size limit are obtained through an efficient microwave-assisted non-aqueous synthesis, offering well-defined nanoparticle building blocks for achieving the targeted ferroelectric functionality. The films prepared from these dispersions by spin coating were sintered and thereby enlarged volume fractions of grain boundaries can be realized, which is of great interest to tune the dielectric and ferroelectric properties over a wider range when compared to classical wet chemical methods such as sol–gel based deposition methods,[42–45] or spray pyrolysis.[46] One of the main parameters on the way to widen the accessible film thickness range is the optimization of the drying process. For this reason, we had a closer look at the drying process and based on these investigations we developed engineering guidelines for the selection of the optimal drying temperature regime to ensure the removal of the organic impurities without cracking. For the deposition Si and Pt/SiO$_2$/Si substrates were chosen, because they are compatible with the conventional Si semiconductor technology. As a proof-of-concept for the functionality of the films, the ferroelectric and optical responses were tested, representing a first step toward future integration of these films into ferroelectric/multiferroic devices.

Results and discussion

BaTiO$_3$ with crystal sizes in the range of 10 nm is synthesized in acetophenone as the solvent.[47] The nanoparticles are large enough to exhibit pronounced ferroelectric properties in contrast to BaTiO$_3$ nanoparticles prepared in benzyl alcohol[48] (although also these small particles of 5 nm exhibited some ferroelectric properties[49]). The as-synthesized nanoparticles are functionalized with 2-(2-(2-methoxyethoxy)ethoxy)acetic acid (MEAAA),[50] transformed into stable dispersions and then used for the deposition of BaTiO$_3$ films with varying thicknesses by several spin-coating and drying cycles. These steps are repeated until the desired thickness is reached. Finally, all films are sintered at 700 °C. The film preparation procedure is summarized in Fig. 2a. A transmission electron microscopy (TEM) image of the as-synthesized nanoparticles and a cross-sectional scanning electron microscopy (SEM) image of the resulting film after sintering are shown in Fig. 2b and c, respectively. X-ray diffraction (XRD) and Raman spectroscopy are employed for the structural analysis of both the as-synthesized nanoparticles and the nanoparticle thin films. All diffraction peaks in the XRD of the nanoparticles and the films can be indexed to the cubic BaTiO$_3$ phase without any crystalline side phases such as BaCO$_3$, Fig. 2d, in agreement with the literature.[54] For comparison, XRD patterns of both powder and thin film samples are recorded using thin film optics to have the same instrumental contribution to peak broadening which, however, reduces the signal-to-noise ratio. The average crystallite size is estimated to be 13 nm and 20 nm using the Scherrer equation on the (110) reflection[55] for the nanoparticles and the films, respectively. In this size regime, it is not possible to differentiate between tetragonal and cubic
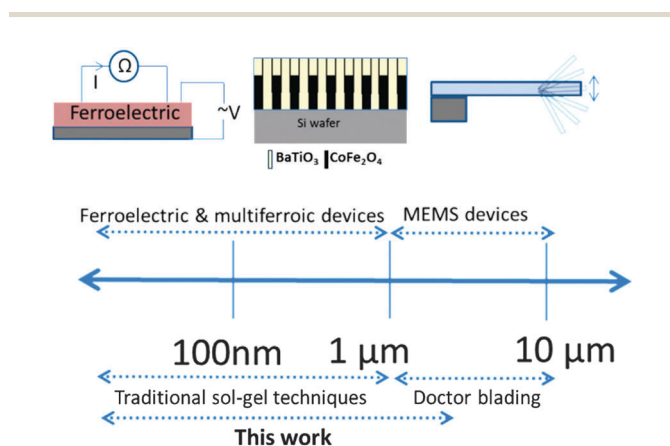

Fig. 1 Overview of various device applications with their required film thicknesses and the corresponding liquid phase deposition for BaTiO$_3$ thin films.
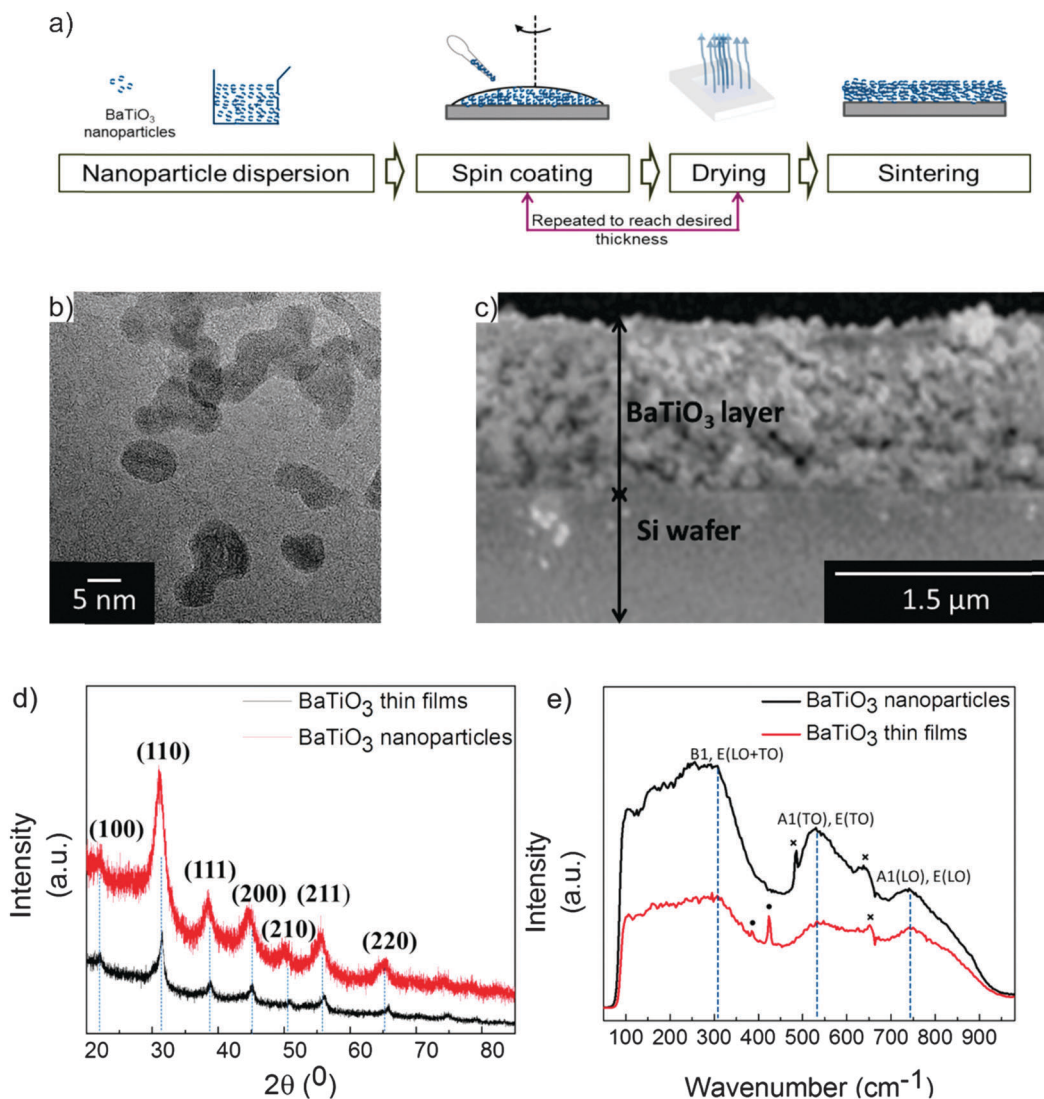
9834 | J. Mater. Chem. C, 2015, 3, 9833–9841

This journal is © The Royal Society of Chemistry 2015

Fig. 2 (a) Flowchart of the film deposition process, (b) TEM image of the as-synthesized $BaTiO_3$ nanoparticles, (c) cross-sectional SEM image of a 1 μm thick $BaTiO_3$ nanoparticle film, (d) XRD of $BaTiO_3$ nanoparticles and nanoparticle films, and (e) Raman spectra of $BaTiO_3$ nanoparticles and nanoparticle films.

$BaTiO_3$ due to the peak broadening at sub-140 nm grain size.[56,57] Hence, we perform Raman spectroscopy to further elucidate the near order characteristics, Fig. 2e.

The nanoparticles and films are characterized by three broad Raman modes at 170 cm^{-1} (A1 mode of T1), 307 cm^{-1} (TO mode of B1), 530 cm^{-1} (TO mode of A1) and 740 cm^{-1} (LO mode of E). These Raman bands are in agreement with the stretching and bending modes for tetragonal $BaTiO_3$, Table 1 and ref. 51. The small Raman peak assigned to the TO mode of B1 exhibits broadening and a lowered intensity in comparison to the Raman spectrum of bulk $BaTiO_3$, indicative for small tetragonal distortions and a generally small particle size. We observe a blue shift for the TO mode of A1 and the LO mode of E in comparison to the single crystal $BaTiO_3$ data pointing to lattice strain.[53] Additional E_{1g} and A_{1g} Raman vibrations marked with an asterisk originate from the presence of additional hexagonal phases of $BaTiO_3$, Table 1.

The co-presence of the hexagonal and tetragonal $BaTiO_3$ phases is reported in the literature for particles with an average

Table 1 Assignment of the observed Raman bands

Raman shift (cm^{-1})	Symmetry	Crystal structure	Nanoparticles	Thin films	Literature
307	B1, E(LO + TO)	Tetragonal	*	*	51
488	E_g	Hexagonal	*	*	52
530	E(TO), A1(TO)	Tetragonal	*	*	53
640	A_{1g}	Hexagonal	*	*	52
740	E(LO), A1(LO)	Tetragonal	*	*	53

size of below 40 nm.[56] The Raman bands marked with a dot in the film spectrum originate from the substrate. We summarize the assignment of all Raman vibrations together with a comparison of literature data in Table 1.

In the following section, we investigate the complex interplay between the organic residues and the drying kinetics for the fabrication of nanoparticle-based $BaTiO_3$ films to elaborate the upper limit of the film thickness accessible by this process. As it is typical for a non-aqueous synthesis route and for a
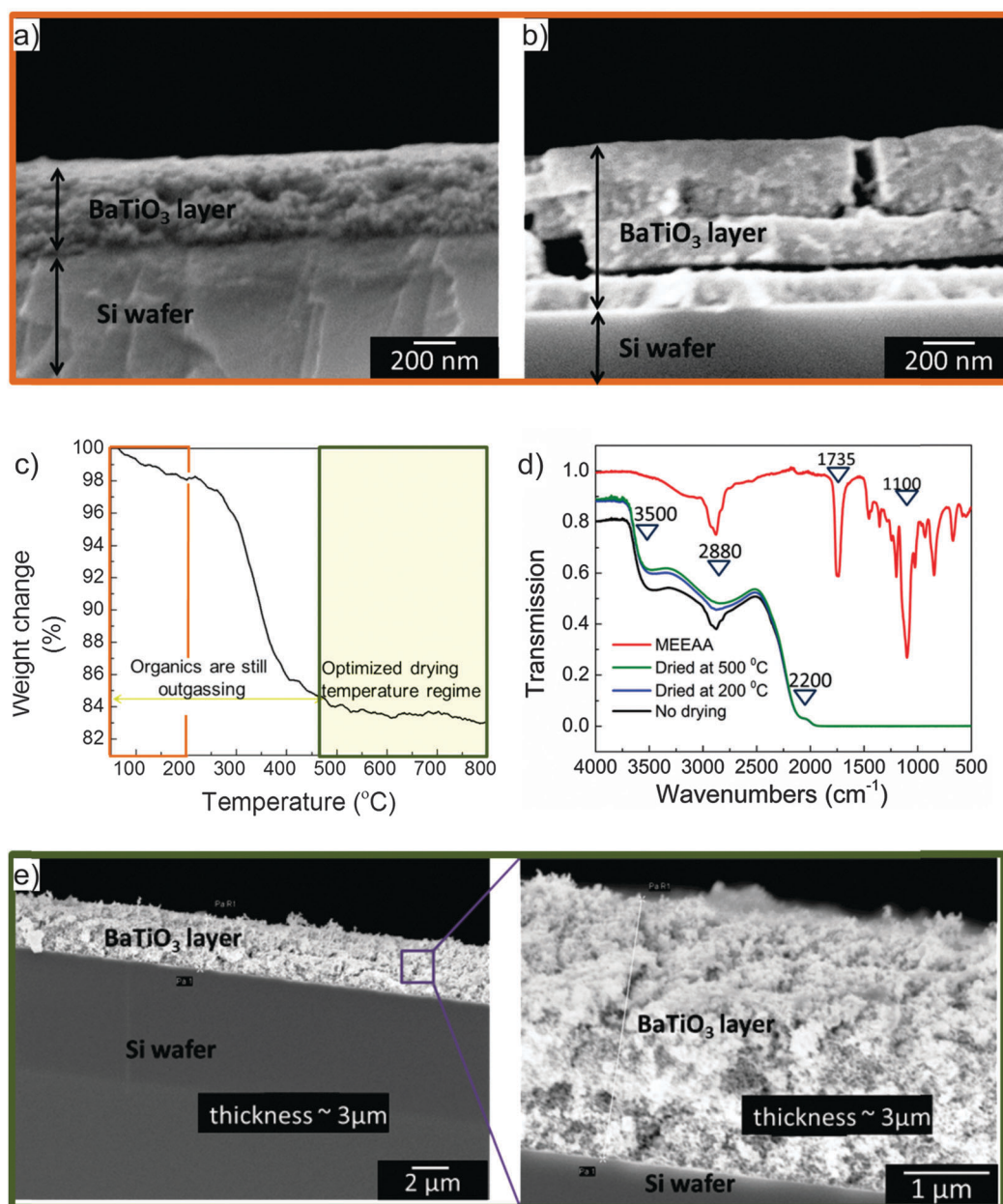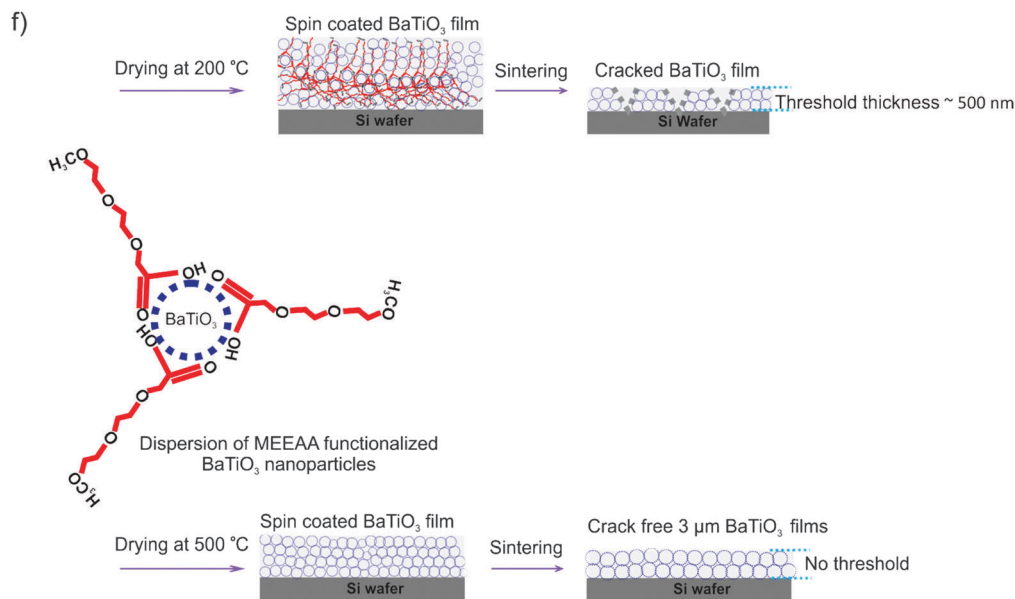
dispersion based on organic solvents, all kinds of organic residues have to be carefully removed to avoid capillary stresses and subsequent cracking of the films during sintering.

To obtain thick films, several spin coating and drying steps are required. Using a dispersion with a nanoparticle concentration of 60 mg ml^{-1} every spin contributes to about 100 nm to the film thickness. According to SEM cross-sectional analysis, a crack-free, approx. 450 nm thick film composed of $BaTiO_3$ nanoparticles was deposited *via* four cycles of spin coating–intermediate drying at 200 °C, followed by a single final sintering at 700 °C, Fig. 3a. The intermediate drying temperature was high enough to ensure evaporation of the dispersing medium (*e.g.* ethanol), enabling the stacking of the $BaTiO_3$ nanoparticles without dissolution of the previous coatings into a multilayer structure. However, delamination between the layers becomes a

problem, when a critical thickness of approx. 500 nm is exceeded after deposition in the 5th cycle, as revealed by the SEM cross-sectional image in Fig. 3b.

To gain a fundamental understanding of the role of drying and compaction in this particular case of nanoparticle deposited films and to give hands on engineering guidance on how to deposit crack-free and micrometer thick films, thermogravimetric analysis (TGA) and Fourier transform infrared (FTIR) spectroscopy were carried out, Fig. 3c and d. In the TGA, up to a temperature of 500 °C, a weight loss of approx. 15 wt% is measured, Fig. 3c. The onset temperature of the main weight loss is around 300 °C, and it is attributed to the outgassing of organics without affecting $BaTiO_3$, which is stable in this temperature range.[58] We analyze the organics in an as-deposited film and in a film dried at 200 °C by transmission FTIR, Fig. 3d.

9836 | *J. Mater. Chem. C*, 2015, **3**, 9833–9841

This journal is © The Royal Society of Chemistry 2015

Fig. 3 Cross-sectional SEM images of (a) 450 nm and (b) 600 nm thick film. (c) TGA graph, (d) FTIR spectra of the films dried at different temperatures, and (e) cross-sectional overview and magnified SEM images of a 3 μm thick film. (f) Schematic drawings showing the effect of incomplete removal of the organics during drying on the microstructure of the films.

Both spectra reveal three absorption bands at 3500 cm^{-1}, 2880 cm^{-1} and below 2200 cm^{-1} (below 2200 cm^{-1} the glass substrate absorbs). We ascribe the first two IR absorption bands observed at higher wavenumbers to the O–H stretching vibrations of adsorbed water,[59] and to aliphatic C–H stretching vibrations[60] originating from the stabilizing agent MEEAA. For comparison, the FTIR spectrum of MEEAA is also shown in Fig. 3c, revealing two additional strong absorption bands in the glass absorption region. These bands at 1735 cm^{-1} and 1100 cm^{-1} belong to C=O and C–O–C vibrations.[61] It is interesting to note that the absence of any absorption bands from the aromatic ring of acetophenone between 3000–3100 cm^{-1} indicates that no acetophenone is bound to the surface of the BaTiO$_3$ nanoparticles. Accordingly, acetophenone does not play any significant role in the drying chemistry. Heating the as-deposited films to 200 °C results in a significant reduction of the IR absorption band intensity for the aliphatic species and for the water vibrations. These absorption band intensities are even more reduced in the sample dried at 500 °C. The outgassing of organics is responsible for the great amount of weight loss observed in Fig. 3c. When dried at 200 °C, MEEAA is still present on the BaTiO$_3$ nanoparticle surfaces. The decomposition of MEEAA mostly takes place during the subsequent sintering of the thin films. Based on TGA and FTIR data we can reasonably relate the premature cracking of the BaTiO$_3$ films during sintering to tensile stresses as a result of the removal of organics. Obviously, a drying temperature of 200 °C is not high enough to remove enough organics to ensure a sintering process without crack formation. On the other hand, for drying or calcination temperatures higher than 500 °C, most organics are removed and the weight loss is below 1 wt% up to a temperature of 800 °C, Fig. 3c. At this point, due to the minor amount of organic

residues cracking stresses are not to be expected anymore. As a proof-of-concept we deposited successfully a crack-free, 3 micrometer thick BaTiO$_3$ film in four consecutive spin coating-calcination steps at a temperature of 500 °C, as shown in the SEM cross-sectional image, Fig. 3e. In general, several experimental parameters have an influence on the final film thickness, for example the spinning speed and time, dispersion concentrations, the number of spin coating-drying cycles, *etc.* In this study, a spinning speed of 1000 rpm and a spinning time of 20 s were found to be optimal and thus kept constant for all films. Higher spinning rates disrupt the film uniformity in the case of low boiling point dispersion media such as ethanol. Therefore, the film thickness was tuned *via* the number of spin coating-drying cycles and/or *via* the concentrations of the dispersions in the range from 50 nm up to 700 nm per deposition (see ESI,† Fig. S1). Atomic force microscopy (AFM) images of the films indicate that the surface roughness is typically in the range of 10 nm, but can be as low as 5 nm (see ESI,† Fig. S2).

Optical band gap and optical properties

The optical properties of the heated BaTiO$_3$ nanoparticle thin films in the visible range are examined *via* their reflectance spectra and compared to the as-synthesized nanoparticles, Fig. 4a. The BaTiO$_3$ nanoparticles exhibit a maximum diffuse reflectance of 75%, whereas the 250 nm thick BaTiO$_3$ films exhibit 23% maximum diffuse reflectance. We calculate the band gaps for the BaTiO$_3$ nanoparticle powder and the films by Tauc plots of $(f(\alpha)h\nu)^2$ and Kubelka–Munk calculations for the absorption coefficients,[62] Fig. 4b. Using this approach, the band gap of the as-synthesized nanoparticles is 3.8 eV and 3.5 eV for the films. Obviously, the BaTiO$_3$ nanoparticles have a significantly increased band gap compared to the bulk value
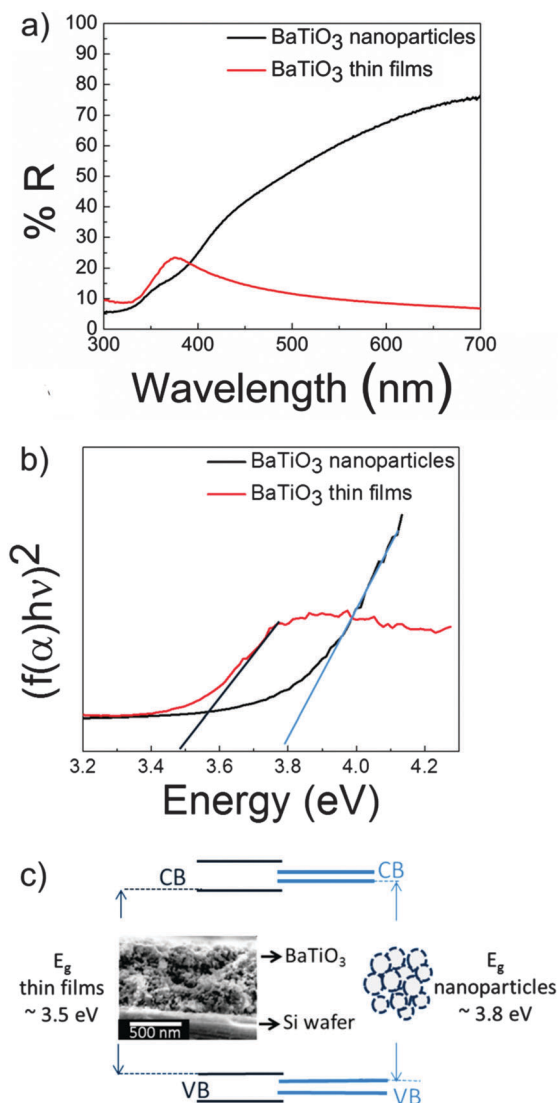
This journal is © The Royal Society of Chemistry 2015

J. Mater. Chem. C, 2015, 3, 9833–9841 | 9837

Fig. 4 (a) UV-vis reflectance spectra, and (b) corresponding Tauc plots of BaTiO$_3$ nanoparticles and nanoparticle-based films. (c) Schematic drawing representing the band gaps E_g of the as-synthesized nanoparticles and sintered thin films.

of 3.2 eV.[63] The nanoparticle powder and the nanoparticle-based films show an increased band gap of +0.3–0.6 eV and are thus of a more electrically insulating nature.

Several effects may play a role in band gap widening in nanomaterials,[63,64] however narrowing of conduction and valence bands originating from the nanocrystalline nature of the films is believed to be the most relevant mechanism for the wider band gap of our system.[65] The large band gap also implicates that the sample is chemically pure, because foreign atoms would decrease the transparency range.[66]

The large band gaps E_g of the BaTiO$_3$ thin films result in outstanding transparency in the visible range, exceeding 90% transparency above 500 nm for films approx. 200 nm and 100 nm thick (Fig. S3a, ESI†). Such optical properties make both, the BaTiO$_3$ nanoparticles and the nanoparticle-based films promising candidates for future devices in the field of

electrooptics[67] and integrated optics, as the single phase as well as the constituent in multiferroic composite materials.[68] A more detailed discussion of the optical characterization and porosity of BaTiO$_3$ films fabricated from dispersions with varying nanoparticle concentrations is given in the ESI,† Fig. S3b and c. The refractive index of the films can be tuned in the range from 1.5–1.8 *via* altering the concentration of the initial colloidal dispersion, while maintaining the extinction coefficients low. Films with different porosities and thus different refractive indices can be deposited by our method. This flexibility facilitates further applications as Bragg-stacks, enables variation of the refractive index contrast by liquid impregnation of the pores and opens up possibilities for sensing.

Ferroelectric switching of nanoparticle-based films

We exemplify and confirm, as a proof-of-concept for the applicability, the local ferroelectric switching behavior of the BaTiO$_3$ films and the corresponding hysteresis loops *via* switching spectroscopy piezoresponse force microscopy (PFM), Fig. 5. For the longitudinal piezoelectric strain coefficient d_{33} (responsible for the longitudinal strains in the case of vertically applied electric fields) a maximum value of 5 pm V^{-1} is measured for *ca.* 200 nm thick BaTiO$_3$ films, Fig. 5a. Despite the crack free microstructure, d_{33} values are limited to a few picometers per volt in this grain size regime, as reported previously for sol gel deposited nanocrystalline BaTiO$_3$ thin films of similar grain sizes,[69] and our findings perfectly agree with the given particle size – piezoresponse arguments. An exact calculation of the piezoelectric coefficient d_{33} from the piezoresponse data is difficult due to the inhomogeneous electric field between the PFM tip and the sample.[70] Additionally, the relatively high
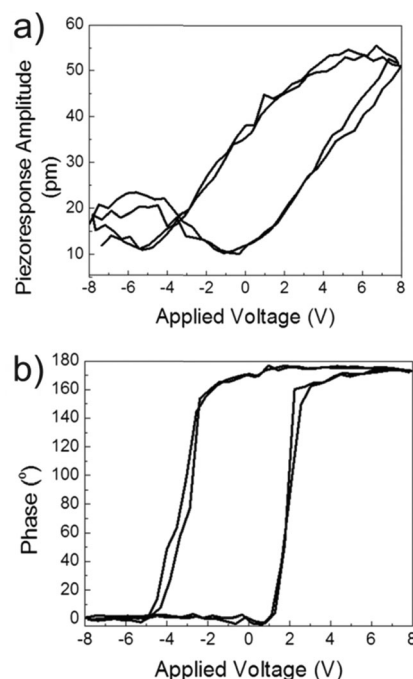

Fig. 5 (a) Amplitude and (b) phase shifts of the piezoresponse local hysteresis loops of BaTiO$_3$ nanoparticle thin films.

9838 | *J. Mater. Chem. C*, 2015, **3**, 9833–9841

This journal is © The Royal Society of Chemistry 2015

shear piezoelectric coefficient, d_{15}, for these materials especially in the case of nanocrystalline thin films[71] causes a significant piezoresponse in the lateral directions in the case of a vertically applied electric field. The full phase shift in the piezoresponse proves that complete switching over 0–180° takes place along the x-axis upon changing the bias polarity, as seen from the response *versus* applied potential curve, Fig. 5b.

In contrast to macroscopic ferroelectric switching measurements reported in the literature,[72] PFM measurements on the films in this work reveal an asymmetric switching profile for which the coercive voltages are close to 1 V for positive bias, and increased coercivity towards a negative bias of 2 V (Fig. 5b). Accordingly, the amplitudes are increased for positive and reduced for negative bias switches (Fig. 5b). We attribute the asymmetric switching profiles to the asymmetric electrical contact during the measurements, where a micro-contact is applied to the top of the film–air interface, and a partial coverage of the macro-contact is employed for the bottom electrode. Hence, work functions of the electrodes may differ for the top and the bottom surface of the film.[73]

Conclusions

This work shows that a colloidal route based on preformed nanoparticles can successfully be applied to the preparation of $BaTiO_3$ films of a broad range of thicknesses from some tenths of nanometers up to a few micrometers. Unlike classic wet-chemical techniques, crystallization is already accomplished by deposition due to the nanocrystalline nature of the colloidal dispersions. Correlation between the dispersing medium ethanol, the dispersant MEEAA and the drying conditions is observed and engineering guidance on how to make crack-free films is provided. An increase in the electronic band gap in comparison to bulk indicates that the films are more insulating, and thus reach an outstanding transparency of more than 90% in the visible range for several hundred nanometer thick films. Such improved characteristics enable a wider operation range for electro-optical devices. A first proof-of-concept for the ferroelectric nature of the nanoparticle-based films is evidenced by switching spectroscopy PFM measurements. The fact that nanoparticle-based films can now be produced over a wider range of thicknesses without cracking, but with high grain interconnectivity and desired ferroelectric and optic properties represents a promising step towards the fabrication of multiferroics and ferroelectrics and applications thereof in random access memory devices by low-cost wet-chemistry approaches.

Experimental procedure

Materials

Dendritic metal pieces of barium (99.99% purity), titanium(ɪᴠ) isopropoxide (99.999% purity), 2-[2-(2-methoxyethoxy)ethoxy]-acetic acid (technical grade) and hexane (>95% purity) were purchased from Aldrich fine chemicals and used without any further purification. Ethanol of 99.8% purity was obtained

from Fluka. Acetophenone (98% purity) was obtained from Acros organics and degassed *via* 3 freeze–thaw cycles before the synthesis. Fused silica, ⟨100⟩ oriented p-type Si wafers, and $Pt/TiO_2/SiO_2/Si$ wafers (MTI Corp, USA) were used for film deposition.

Synthesis of particles and dispersions

The synthesis is a combination and adaptation of previously reported protocols.[47,74] In a typical synthesis, 137 mg of dendritic Ba is dissolved in 5 ml of degassed acetophenone at 80 °C in an argon filled glove box, followed by dropwise addition of a molar equivalent of titanium isopropoxide. The mixture is transferred to a microwave vial, sealed and exposed to microwave irradiation for 30 minutes at a synthesis temperature of 220 °C using a CEM Discovery reactor.

The nanoparticles are centrifuged off, washed twice with ethanol and finally sonicated for 45 minutes in 5 ml of 0.3 M ethanolic MEEAA solution using a Branson B3510 ultrasonic cleaner. After sonication, the nanoparticles are stirred overnight in this mixture to ensure sufficient binding of the stabilizing molecules to the nanoparticle surfaces. In the following step, an excessive amount of hexane (5 : 1 hexane to ethanol ratio in volume) is added and the mixture is centrifuged in order to separate the nanoparticles from excess stabilizing agents. Afterwards, the $BaTiO_3$ nanoparticles are re-dispersed in ethanol with a subsequent sonication step.

Synthesis of films

$BaTiO_3$ nanoparticle thin films are fabricated using spin coating with intermediate drying at 200 °C or 500 °C at a maximum spinning speed of 1000 rpm in a total spinning period of 20 seconds using a Laurell WS650 spin coater. Typically, the concentrations of the nanoparticle dispersions are altered between 30 and 250 mg ml^{-1} to obtain thickness values per spin coating between approx. 50 and 750 nm. To deposit a 3 μm thick film, 4 spin coating cycles with 500 °C intermediate drying are carried out, followed by a final sintering step using nanoparticle dispersions of 250 mg ml^{-1} initial concentration. All film deposition processes prior to sintering are carried out in a laminar flow controlled, synthetic air filled glovebox. The sintering step at the very end of all spin coating-drying cycles was performed at 700 °C for 2 hours in air with 4 hours of ramping (approx. 2.8 °C min^{-1} ramping rate) in a Nabertherm L 3/11/B170 laboratory muffle furnace.

Characterization

SEM images were obtained from films deposited on Si wafers at an operational voltage of 3–5 kV using a LEO 1530 scanning electron microscope. Transmission electron microscopy (TEM) studies were performed on a FEI Tecnai F30 FEG operating at 300 kV. Powder and film XRD patterns were obtained using a PANalytical X'Pert Pro diffractometer with a Cu Kα source in grazing incidence geometry between 20–85° using 50 seconds per step and a step size of 0.01° and 0.0065° for thin films and powders, respectively. To investigate the near order characteristics of the films and nanoparticles, a WITec CRM200 Confocal

Raman Microscope with a green laser of 532 nm was employed. Thermogravimetric analysis was carried out on post-synthesis functionalized powders and films dried at 200 °C using a Mettler Toledo TGA/SDTA851. Samples were heated from 50 °C to 800 °C at a heating rate of 5 °C min⁻¹ under air. FT-IR spectroscopy was performed on a Bruker Alpha FT-IR Spectrometer on undried, and 200 °C and 500 °C dried thin film samples on glass substrates. UV-vis spectra were obtained using a JASCO V-770 spectrophotometer with an ILN-725 integrating sphere accessory with background subtraction and with respect to standard $BaSO_4$ powder. Topography images were obtained in intermittent contact mode AFM of an Asylum Cypher™ using AC160TS-R3 tips and surface roughness was calculated accordingly. The ferroelectric properties were investigated in DART-SSPFM mode of an Asylum Cypher™ using doped diamond PFM tips from NDMDT on films deposited on $Pt/TiO_2/SiO_2/Si$ substrates with the Pt bottom electrode being ground during the measurements. Deflection in volts and thermal calibration of the tips were done prior to PFM measurements and the presented hysteresis curves were obtained in the remnant mode to minimize electromechanical tip–sample interactions with an ac reading voltage of 1 V.

Acknowledgements

References

1 P. Navuduri, I. M. Abdel-Motaleb, Y. Z. Yoo and O. Chmaissem, ICSICT-2006: *8th International Conf. on Solid-State and Integrated Circuit Technology Proc.*, 2007, 1004–1006.

2 R. W. Schwartz, T. Schneller and R. Waser, *C. R. Chimie*, 2004, **7**, 433–461.

3 E. F. Alberta and W. S. Hackenberger, *AIP Conf. Proc.*, 2006, 375–383.

4 M. J. Pan and C. Randall, *IEEE Electr. Insul. Mag.*, 2010, **26**, 44–50.

5 R. Ashiri, A. Nemati and M. Sasani Ghamsari, *Ceram. Int.*, 2014, **40**, 8613–8619.

6 X. Chen, C. H. Jia, Y. H. Chen, G. Yang and W. F. Zhang, *J. Phys. D: Appl. Phys.*, 2014, **47**, 36.

7 R. V. Chopdekar, V. K. Malik, A. Fraile Rodríguez, L. Le Guyader, Y. Takamura, A. Scholl, D. Stender, C. W. Schneider, C. Bernhard, F. Nolting and L. J. Heyderman, *Phys. Rev. B: Condens. Matter Mater. Phys.*, 2012, **86**, 014408.

8 R. Grigalaitis, M. M. Vijatović Petrović, J. D. Bobić, A. Dzunuzovic, R. Sobiestianskas, A. Brilingas, B. D. Stojanović and J. Banys, *Ceram. Int.*, 2014, **40**, 6165–6170.

9 H. Zhang, X. H. Wang, Z. B. Shen and Y. N. Hao, *Adv. Mater. Res.*, 2014, **833**, 8–12.

10 Z. Liu, P. T. Lin and B. W. Wessels, *J. Opt. A: Pure Appl. Opt.*, 2008, **10**, 015302.

11 Z. Liu, P. T. Lin, B. W. Wessels, F. Yi and S. T. Ho, *Appl. Phys. Lett.*, 2007, **90**, 201104.

12 N. Spaldin, Analogies and Differences between Ferroelectrics and Ferromagnets, *Physics of Ferroelectrics*, Springer, Berlin, Heidelberg, 2007, pp. 194–200.

13 X. Y. Wang, Y. L. Wang and R. J. Yang, *Appl. Phys. Lett.*, 2009, **95**, 142910.

14 M. Ahmadi, N. Phonthammachai, T. H. Shuan, T. J. White, N. Mathews and S. G. Mhaisalkar, *Org. Electron.*, 2010, **11**, 1660–1667.

15 W. Ousi-Benomar, S. S. Xue, R. A. Lessard, A. Singh, Z. L. Wu and P. K. Kuo, *J. Mater. Res.*, 1994, **9**, 970–979.

16 T. Dechakupt, S. Ko, S.-G. Lu, C. Randall and S. Trolier-McKinstry, *J. Mater. Sci.*, 2011, **46**, 136–144.

17 E. G. Bakhoum and M. H. M. Cheng, *J. Microelectromech. Syst.*, 2010, **19**, 443–450.

18 N. Dai, G. J. Hu, X. K. Hong and J. L. Shang, SPIE 6984, Sixth International Conf. on Thin Film Physics and Applications, 2008, 69841X.

19 R. Dorey, in *Ceramic Thick Films for MEMS and Microdevices*, ed. R. Dorey, William Andrew Publishing, Oxford, 2012, ch. 2, pp. 35–61.

20 J. He, J. C. Jiang, J. Liu, G. Collins, C. L. Chen, B. Lin, V. Giurgiutiu, R. Y. Guo, A. Bhalla and E. I. Meletis, *J. Nanosci. Nanotechnol.*, 2010, **10**, 6245–6250.

21 A. Ianculescu, B. Despax, V. Bley, T. Lebey, R. Gavrilă and N. Drăgan, *J. Eur. Ceram. Soc.*, 2007, **27**, 1129–1135.

22 C. H. Jung, S. I. Woo, Y. S. Kim and K. S. No, *Thin Solid Films*, 2011, **519**, 3291–3294.

23 T. Osumi, M. Nishide, H. Funakubo, H. Shima, K. Nishida and T. Yamamoto, *Integr. Ferroelectr.*, 2012, **133**, 42–48.

24 P. S. Patil, *Mater. Chem. Phys.*, 1999, **59**, 185–198.

25 J. L. M. Rupp, B. Scherrer, N. Schäuble and L. J. Gauckler, *Adv. Funct. Mater.*, 2010, **20**, 2807–2814.

26 B. Scherrer, S. Heiroth, R. Hafner, J. Martynczuk, A. Bieberle-Hütter, J. L. M. Rupp and L. J. Gauckler, *Adv. Funct. Mater.*, 2011, **21**, 3967–3975.

27 M. Kosec, D. Kuscer and J. Holc, *Multifunctional Polycrystalline Ferroelectric Materials*, Springer, Netherlands, 2011, ch. 2, vol. 140, pp. 39–61.

28 D. Birnie, III, in *Chemical Solution Deposition of Functional Oxide Thin Films*, ed. T. Schneller, R. Waser, M. Kosec and D. Payne, Springer, Vienna, 2013, ch. 11, pp. 263–274.

29 J. Ba, J. Polleux, M. Antonietti and M. Niederberger, *Adv. Mater.*, 2005, **17**, 2509–2512.

30 J. M. Szeifert, J. M. Feckl, D. Fattakhova-Rohlfing, Y. Liu, V. Kalousek, J. Rathousky and T. Bein, *J. Am. Chem. Soc.*, 2010, **132**, 12605–12611.

31 K. Fominykh, J. M. Feckl, J. Sicklinger, M. Döblinger, S. Böcklein, J. Ziegler, L. Peter, J. Rathousky, E.-W. Scheidt, T. Bein and D. Fattakhova-Rohlfing, *Adv. Funct. Mater.*, 2014, **24**, 3123–3129.

32 A. Aboulaich, O. Lorret, B. Boury and P. H. Mutin, *Chem. Mater.*, 2009, **21**, 2577–2579.

33 C. Grote, T. A. Cheema and G. Garnweitner, *Langmuir*, 2012, **28**, 14395–14404.

34 J. H. Prosser, T. Brugarolas, S. Lee, A. J. Nolte and D. Lee, *Nano Lett.*, 2012, **12**, 5287–5291.

35 C. J. Brinker, in *Chemical Solution Deposition of Functional Oxide Thin Films*, ed. T. Schneller, R. Waser, M. Kosec and D. Payne, Springer, Vienna, 2013, ch. 10, pp. 233–261.

36 K. T. Cook, K. E. Tettey, R. M. Bunch, D. Lee and A. J. Nolte, *ACS Appl. Mater. Interfaces*, 2012, **4**, 6426–6431.

37 C. S. Thompson, R. A. Fleming and M. Zou, *Sol. Energy Mater. Sol. Cells*, 2013, **115**, 108–113.

38 S. Colodrero, M. Ocaña and H. Míguez, *Langmuir*, 2008, **24**, 4430–4434.

39 M. E. Calvo, S. Colodrero, T. C. Rojas, J. A. Anta, M. Ocaña and H. Míguez, *Adv. Funct. Mater.*, 2008, **18**, 2708–2715.

40 D. P. Puzzo, L. D. Bonifacio, J. Oreopoulos, C. M. Yip, I. Manners and G. A. Ozin, *J. Mater. Chem.*, 2009, **19**, 3500–3506.

41 L. Luo, D. Bozyigit, V. Wood and M. Niederberger, *Chem. Mater.*, 2013, **25**, 4901–4907.

42 R. Ashiri, A. Nemati and M. Sasani Ghamsari, *Ceram. Int.*, 2014, **40**, 8613–8619.

43 Y. Chang, R. Xue and Y. Wang, *IEEE Trans. Electron Devices*, 2014, **61**, 4090–4097.

44 P. Ferreira, R. Z. Hou, A. Wu, M.-G. Willinger, P. M. Vilarinho, J. Mosa, C. Laberty-Robert, C. Boissière, D. Grosso and C. Sanchez, *Langmuir*, 2011, **28**, 2944–2949.

45 H. B. Sharma, *Ferroelectrics*, 2013, **453**, 113–121.

46 R. Ayouchi, F. Martín, J. R. Ramos-Barrado and D. Leinen, *Surf. Interface Anal.*, 2000, **30**, 565–569.

47 M. Niederberger and G. Garnweitner, *Mater. Res. Soc. Symp. Proc.*, 2005, 192–196.

48 M. Niederberger, G. Garnweitner, N. Pinna and M. Antonietti, *J. Am. Chem. Soc.*, 2004, **126**, 9120–9126.

49 K. Page, T. Proffen, M. Niederberger and R. Seshadri, *Chem. Mater.*, 2010, **22**, 4386–4391.

50 D. Taroata, W. Fischer, T. A. Cheema, G. Garnweitner and G. Schmid, *IEEE Trans. Dielectr. Electr. Insul.*, 2012, **19**, 298–304.

51 M. B. Smith, K. Page, T. Siegrist, P. L. Redmond, E. C. Walter, R. Seshadri, L. E. Brus and M. L. Steigerwald, *J. Am. Chem. Soc.*, 2008, **130**, 6955–6963.

52 K. Tsuzuku and M. Couzi, *J. Mater. Sci.*, 2012, **47**, 4481–4487.

53 H. Z. Guo, Z. H. Chen, B. L. Cheng, H. B. Lu, L. F. Liu and Y. L. Zhou, *J. Eur. Ceram. Soc.*, 2005, **25**, 2347–2352.

54 A. Bele, M. Cazacu, G. Stiubianu and S. Vlad, *RSC Adv.*, 2014, **4**, 58522–58529.

55 S. H. Jhung, J.-H. Lee, J. W. Yoon, Y. K. Hwang, J.-S. Hwang, S.-E. Park and J.-S. Chang, *Mater. Lett.*, 2004, **58**, 3161–3165.

56 M. Yashima, T. Hoshina, D. Ishimura, S. Kobayashi, W. Nakamura, T. Tsurumi and S. Wada, *J. Appl. Phys.*, 2005, **98**, 014313.

57 E. Zolotoyabko, J. L. M. Rupp and L. J. Gauckler, *Scr. Mater.*, 2012, **66**, 190–193.

58 M. Ejaz, V. S. Puli, R. Elupula, S. Adireddy, B. C. Riggs, D. B. Chrisey and S. M. Grayson, *J. Polym. Sci., Part A: Polym. Chem.*, 2015, **53**, 719–728.

59 R. Ashiri, *Metall. Mater. Trans. A*, 2012, **43**, 4414–4426.

60 D. Olmos, E. V. Martin and J. Gonzalez-Benito, *Phys. Chem. Chem. Phys.*, 2014, **16**, 24339–24349.

61 T. A. Cheema and G. Garnweitner, *CrystEngComm*, 2014, **16**, 3366–3375.

62 D. K. Takci, E. Senadim Tuzemen, K. Kara, S. Yilmaz, R. Esen and O. Baglayan, *J. Mater. Sci.: Mater. Electron.*, 2014, **25**, 2078–2085.

63 Y. Garbovskiy and A. Glushchenko, *Appl. Opt.*, 2013, **52**, E34–E39.

64 S. Ramakanth and K. C. James Raju, *J. Appl. Phys.*, 2014, **115**, 173507.

65 J. S. Zhu, X. M. Lu, W. Jiang, W. Tian, M. Zhu, M. S. Zhang, X. B. Chen, X. Liu and Y. N. Wang, *J. Appl. Phys.*, 1997, **81**, 1392–1395.

66 Y. Garbovskiy and A. Glushchenko, *Appl. Opt.*, 2013, **52**, E34–E39.

67 W. H. P. Pernice, X. Chi, F. J. Walker and H. X. Tang, *IEEE Photonics Technol. Lett.*, 2014, **26**, 1344–1347.

68 S. Roy and S. B. Majumder, *J. Appl. Phys.*, 2012, **112**, 043520.

69 K. Tanaka, K. Suzuki, D. Fu, K. Nishizawa, T. Miki and K. Kato, *Jpn. J. Appl. Phys., Part 1*, 2004, **43**, 6525–6529.

70 T. Jungk, Á. Hoffmann and E. Soergel, in *Ferroelectric Crystals for Photonic Applications*, ed. P. Ferraro, S. Grilli and P. De Natale, Springer, Berlin, Heidelberg, 2014, ch. 8, vol. 91, pp. 205–226.

71 P. Ferreira, R. Z. Hou, A. Wu, M. G. Willinger, P. M. Vilarinho, J. Mosa, C. Laberty-Robert, C. Boissière, D. Grosso and C. Sanchez, *Langmuir*, 2012, **28**, 2944–2949.

72 C. L. Li, Z. H. Chen, Y. L. Zhou and D. F. Cui, *J. Phys.: Condens. Matter*, 2001, **13**, 5261–5268.

73 A. Gruverman, A. Kholkin, A. Kingon and H. Tokumoto, *Appl. Phys. Lett.*, 2001, **78**, 2751–2753.

74 I. Bilecka, I. Djerdj and M. Niederberger, *Chem. Commun.*, 2008, 886–888.